

# High-Quality Perovskite Films Grown with a Fast Solvent-Assisted Molecule Inserting Strategy for Highly Efficient and Stable Solar Cells

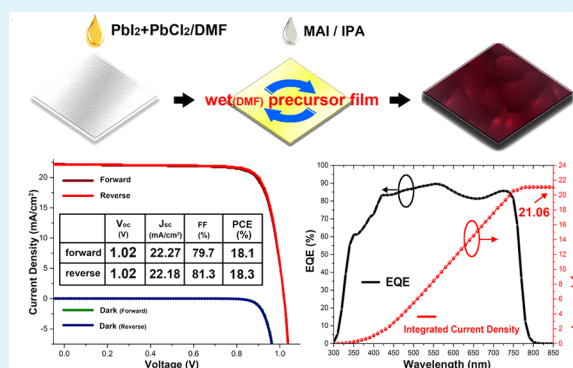
Shuai Yuan,<sup>†</sup> Zhiwen Qiu,<sup>†</sup> Chaomin Gao,<sup>‡</sup> Hailiang Zhang,<sup>†</sup> Yanan Jiang,<sup>†</sup> Cuncheng Li,<sup>‡</sup> Jinghua Yu,<sup>‡</sup> and Bingqiang Cao<sup>\*,†</sup>

<sup>†</sup>Materials Research Center for Energy and Photoelectrochemical Conversion, School of Material Science and Engineering, and <sup>‡</sup>School of Chemistry and Chemical Engineering, University of Jinan, Jinan 250022, Shandong, China

## Supporting Information

**ABSTRACT:** The performance of organolead halide perovskites based solar cells has been enhanced dramatically due to the morphology control of the perovskite films. In this paper, we present a fast solvent-assisted molecule inserting (S-AMI) strategy to grow high-quality perovskite film, in which the methylammonium iodide/2-propanol (MAI/IPA) solution is spin-coated onto a dimethylformamide (DMF) wetted mixed lead halide ( $\text{PbX}_2$ ) precursor film. The DMF can help the inserting of MAI molecules into the  $\text{PbX}_2$  precursor film and provide a solvent environment to help the grain growth of the perovskite film. The perovskite film grown by the S-AMI approach shows large and well-oriented grains and long carrier lifetime due to the reduced grain boundary. Solar cells constructed with these perovskite films yield an average efficiency over 17% along with a high average fill factor of 80%. Moreover, these unsealed solar cell devices exhibit good stability in an ambient atmosphere.

**KEYWORDS:** perovskite, solar cell, morphology, large grains, solution process, long-term stability



## INTRODUCTION

Photovoltaic devices that convert solar energy to electricity are one of the most promising technologies for renewable energy. In recent years, photovoltaic cells based on organolead halide perovskite film materials have attracted enormous attention. The power conversion efficiency (PCE) over 20% was already certified for small-area devices,<sup>1</sup> which assures that the organolead halide perovskite solar cell is one of the most promising candidates for next-generation solar cells. One of the reasons for the high PCE of perovskite solar cell is the continuously improving material preparation process and perovskite film quality.<sup>2–8</sup> In attempting to obtain superb perovskite film, different deposition methods and according precursor additives are under intense study.<sup>9–15</sup> Several strategies have been successfully applied to improve the quality of the multicrystalline film prepared by both one-step and two-step approaches.<sup>16–22</sup> The solvent engineering method is a representative example by which high-quality perovskite films can be grown using the one-step method.<sup>17,18</sup> The two-step interdiffusion method developed by Xiao et al. shows superior perovskite film morphology and solar cell device performances.<sup>19–22</sup> In attempting to further develop this promising method, several additives like  $\text{H}_2\text{O}$ ,<sup>23</sup> phenyl- $\text{C}_{61}$ -butyric acid methyl ester (PCBM),<sup>24</sup> dimethyl sulfoxide (DMSO),<sup>25</sup> and  $\text{H}_3\text{PO}_2$ <sup>26</sup> have been added into the precursor. Recently, a systematic study about the multicycle solution coating process was also reported, which exhibits a strong correlation between

material process and morphology providing a guideline to enhance device performance.<sup>27</sup>

For the conventional interdiffusion (CID) method,  $\text{PbI}_2$  and methylammonium iodide (MAI) are first dissolved in dimethylformamide (DMF) and 2-propanol (IPA), respectively.<sup>19</sup> The precursor solutions are spun onto substrate to form a bilayer structure with a  $\text{PbI}_2$  layer underneath MAI layer. Notably, before spin-coating the upper layer of MAI, the  $\text{PbI}_2$  precursor film is usually heated at 70 or 100 °C to remove the residual solvent (DMF). Then the solution of MAI/IPA is dropped onto the center of  $\text{PbI}_2$  film, and the final perovskite film will be obtained after a second annealing process to promote the interdiffusion and reaction between  $\text{PbI}_2$  and MAI. There is no doubt that IPA and DMF are considered as a matched orthogonal solvent couple for  $\text{PbX}_2$  ( $X = \text{I}, \text{Cl}, \text{Br}$ ). Since  $\text{PbX}_2$  has relatively low solubility in IPA, the spin coating of MAI/IPA induces no impact to  $\text{PbX}_2$ .<sup>9</sup> On the contrary, MAI can dissolve into both of those two solvents (DMF and IPA). In addition, as a universal solvent, DMF possess a superb intersolubility with almost every organic reagent including IPA.

Here, we report a new solvent-assisted molecule inserting strategy (S-AMI) to grow high-quality perovskite film with large grain, reduced trap density, and long carrier lifetime by

Received: June 8, 2016

Accepted: August 16, 2016

Published: August 16, 2016

employing a fresh wet  $\text{PbX}_2$  precursor film. We suppose that the residual DMF in the wet  $\text{PbX}_2$  film will mix with the solution of MAI/IPA and promote the MAI molecule to penetrate into  $\text{PbX}_2$  film resulting a perovskite film with particularly uniform crystallinity and morphology. Meanwhile, the total preparation time for such a perovskite film is only limited within 10 min. Our results demonstrate that the solar cells fabricated by S-AMI show an average PCE over 17% with average fill factor over 80%. Moreover, large active area ( $1 \text{ cm}^2$ ,  $10 \text{ mm} \times 10 \text{ mm}$ ) devices with the best PCE over 13% were also realized with the S-AMI method. In addition, these solar cell devices exhibit good stability in ambient condition (RH  $\sim$  25%) without encapsulation.

## EXPERIMENTAL SECTION

**Precursor Solution Preparation and Perovskite Films Deposition.** Patterned FTO glass with a sheet resistance of  $15 \Omega \text{ sq}^{-1}$  was purchased from Nippon Glass. The aqueous solution of PEDOT:PSS (1.3–1.7 wt %, Heraeus-Clevios PVP AI 4083) and  $\text{PC}_{61}\text{BM}$  (>99%) were obtained from Xi'an Polymer Light Technology Corp. 2,9-Dimethyl-4,7-diphenyl-1,10-phenanthroline (BCP) with purity of 99.8% was obtained from Aladdin. All of other reagents were purchased from Sigma-Aldrich.  $\text{CH}_3\text{NH}_3\text{I}$  was prepared as described in our previous report.<sup>28</sup>  $\text{PbI}_2$  and  $\text{PbCl}_2$  (99.999%, Alfa Aesar) were dissolved in DMF (1 mol/L) with different molar ratios (1:0, 1:1, 2:1, 4:1, and 8:1), where the upper limit molar ratio of  $\text{PbI}_2$ : $\text{PbCl}_2$  was set at 1:1 because of low solubility of  $\text{PbCl}_2$ . Both precursor solutions were heated at  $70 \text{ }^\circ\text{C}$  and stirring overnight. MAI solutions were obtained by dissolving MAI powder in IPA with concentrations at 55, 70, and 85 mg/mL. For the CID method, the  $\text{PbX}_2$  solution was spin-coated on glass substrates at 6000 rpm for 30 s, and the fresh precursor film was transformed onto a hot plate quickly and dried at  $100 \text{ }^\circ\text{C}$  for 5 min. After the  $\text{PbX}_2$  film cooling down to the room temperature, MAI solution was spun onto the precursor film at 6000 rpm for 30 s. The precursor film got a change in color from deep yellow to light brown as the MAI solution dropping onto it. The perovskite film was obtained by annealing the spin-coated  $\text{PbX}_2$ /MAI bilayer at  $100 \text{ }^\circ\text{C}$  for an optimized time of 30 min. For the S-AMI method,  $\text{PbX}_2$  solution was spun on substrate at 6000 rpm for 15 s, and then a drop of MAI solution was dripped onto the center of spin-coated wet precursor film for 30 s without annealing. It should be noted that it would have left a pit on the surface of the as-prepared film if MAI solution dropped too early. The film color transformed from light yellow to deep brown immediately. Finally, varied annealing duration (10, 30, and 60 min) at  $100 \text{ }^\circ\text{C}$  was employed.

**Perovskite Film Characterizations.** Perovskite films coated on glass substrates using the same preparation process as the corresponding solar cells were carried out for scanning electron microscope (SEM), X-ray diffraction (XRD), optical absorption, steady-state photoluminescence (PL), and time-resolve photoluminescence (TRPL) measurements. The SEM images were obtained using a Quanta FEG250 field emission scanning electron microscope. XRD patterns were obtained on an X-ray diffractometer (D8 Advance, Bruker) using  $\text{Cu K}\alpha$  radiation. The UV–visible (UV–vis) optical absorption spectrum was measured with a Shimadzu UV-3600 spectrophotometer and the incident light came from perovskite film side. PL and TRPL measurements were acquired using an FLS920 fluorescence spectrometer (Edinburgh Instruments). For TCSPC measurements, a 509.6 nm pulsed diode laser (EPL-515, pulse width 148.8 ps) with fluency of  $\sim 30 \text{ nJ/cm}^2$  was used to excite the samples impinging on the glass substrate side.

**Device Fabrication and Characterizations.** Fluorine-doped tin oxide (FTO)-coated glass substrate was patterned by etching with Zn powder and HCl diluted in distilled water. The etched substrate was then cleaned with ethanol, saturated KOH solution in isopropanol, and water and then dried with clean dry  $\text{N}_2$ . PEDOT:PSS was spin-coated on the patterned FTO glass substrates at 5000 rpm for 30 s and then dried at  $130 \text{ }^\circ\text{C}$  for 10 min. PEDOT:PSS-coated substrates were

moved to a glovebox (MIKROUNA). Perovskite film was deposited on the PEDOT:PSS-coated substrate as described above. After coating the perovskite film, a  $\text{PC}_{61}\text{BM}$  solution of 20 mg/mL in chlorobenzene was spin-coated onto it at 2000 rpm for 30 s. Then a layer of BCP was deposited at 4000 rpm for 30 s by using a 0.5 mg/mL ethyl alcohol solution to improve the ohmic contact between  $\text{PC}_{61}\text{BM}$  and Ag electrode. The device was finished by thermal evaporating Ag (50 nm) electrodes. The device area is defined to be the overlap of the FTO and silver electrodes.

A Keithley SourceMeter 2612A was employed to measure the current density versus voltage ( $J$ – $V$ ) characteristics of solar cells (from forward to reverse and from reverse to forward) in the dark or under simulated AM 1.5G irradiation ( $100 \text{ mW/cm}^2$ ) using a solar simulator (San-Ei, 3A, 150 W). Before measurement the lamp was turned on for 15 min and the exact light intensity was calibrated using a NREL-traceable KG5 filtered silicon reference cell. The compliance was set at 3 mA, and the scanning step was  $0.3 \text{ V/s}$  without delay time. To testing the maximum-power output stability of the solar cells, a bias voltage at the maximum power of device was used, and the output current is converted to output power by using the following relation:  $\text{PCE} = [J (\text{mA/cm}^2) \times V (\text{V})] / [100 (\text{mW/cm}^2)]$ . The external quantum efficiency (EQE) spectrum was measured using a QEX10 photoresponse system (PV Measurement Inc.). The wavelength interval is 10 nm, and the intensity of the incident light from the monochromator was calibrated using a Si photodiode installed inside (1H002). The beam size of the incident light is smaller than devices area. All measurements were performed under ambient atmosphere with relative humidity of 25%, and solar cells were tested without any encapsulation. Devices stored in a drybox were further measured for stability study.

## RESULTS AND DISCUSSION

The experimental processes of the S-AMI and CID methods are shown in Figure 1. Mixed  $\text{PbI}_2$  and  $\text{PbCl}_2$  precursor was dissolved in DMF at 1 mol/L and spin-coated on top of PEDOT:PSS at 6000 rpm. DMF is known as a solvent with

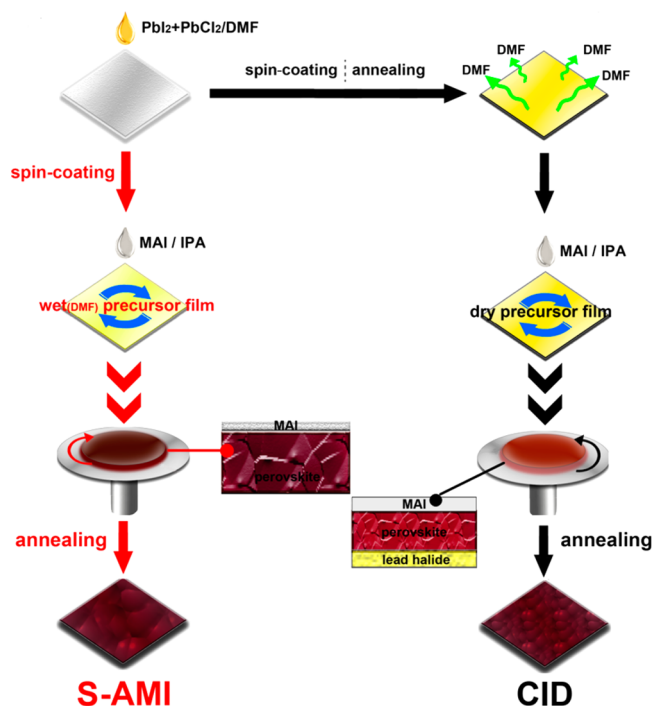


**Figure 1.** Perovskite film growth process schematics comparison. Both starting from spin-coating  $\text{PbX}_2$ /DMF solution, the red and black arrows represent the experimental procedure of the S-AMI and CID methods, respectively.

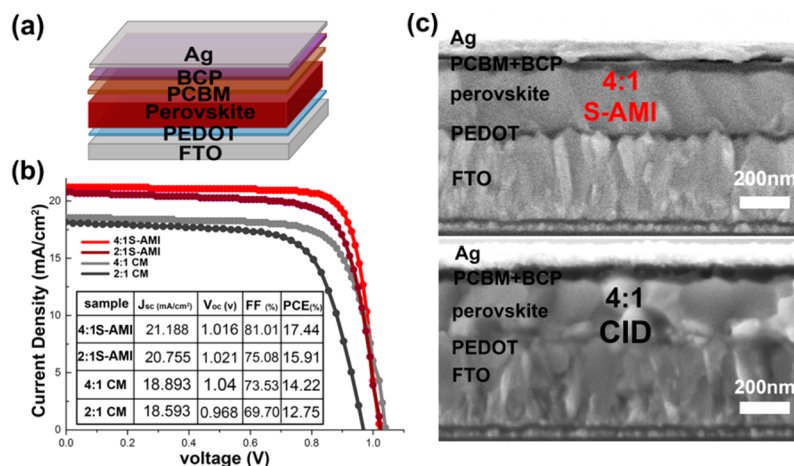


**Figure 2.** (a) Device architecture schematic used in this study. (b) Current density–voltage ( $J$ – $V$ ) curves of devices with perovskite films synthesized by S-AMI or CID. 4:1 or 2:1 symbolizes the molar ratio of  $PbI_2:PbCl_2$ . All devices were measured under AM 1.5G solar irradiation of  $100 \text{ mW/cm}^2$  with scan rate fixed at  $0.3 \text{ V/s}$  and  $0 \text{ s}$  delay time. (c) Cross-sectional SEM images of 4:1 S-AMI and 4:1 CID devices.

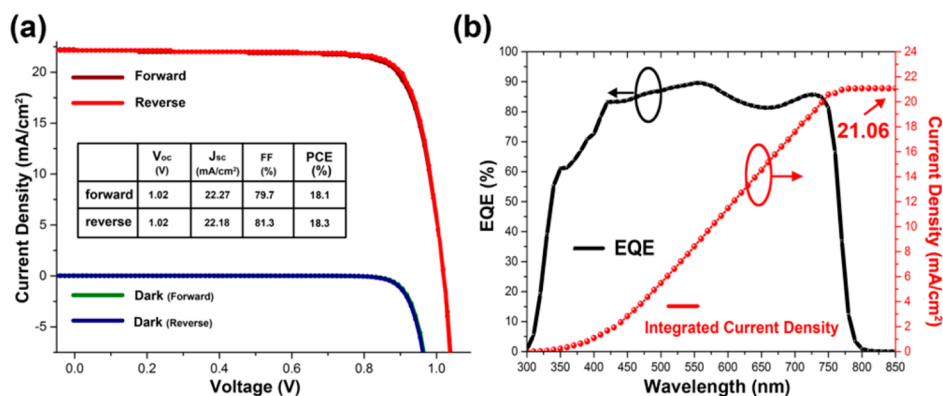


**Figure 3.** (a)  $J$ – $V$  curves (under light and dark) of the champion cell (4:1 S-AMI) with different scanning direction (forward and reverse). The scan rate is  $0.3 \text{ V/s}$  without delay times. (b) The corresponding EQE and integrated current density of the best device.

high boiling point about  $153 \text{ }^\circ\text{C}$  in a normal atmosphere. Therefore, a completely dry  $PbX_2$  film cannot form only after a spin-coating process for few tens of seconds. As for the S-AMI approach, the MAI/IPA solution ( $30 \mu\text{L}$ ) was dropped onto the center of spinning  $PbX_2$  film at around  $15 \text{ s}$ , when the  $PbX_2$  is still wet. The fresh  $PbX_2$  film with a certain amount of DMF is quite transparent and exhibits brilliant yellow in color, which shows similar appearance as the precursor solution but different from its annealed counterpart as shown in Figure S1a,b (Supporting Information). The XRD measurement were carried out immediately after coating  $PbX_2$  films in order to avoid the impact from the volatilization of residual DMF in wetted sample, as shown in Figure S1e. The wetted  $PbX_2$  film shows amorphous and quasi-solution phase, while a narrow (001) peak from crystalline  $PbI_2$  is clearly observed. After the MAI/IPA solution dropped onto the precursor film, the color of the wet  $PbX_2$  film changed from yellow to dark brown immediately, while the color of the dried  $PbX_2$  film changed only slightly (Figure S1a–d). We then adopt XRD, optical absorption spectra, SEM, and steady-state photoluminescence (PL) to study the samples evolution before and after annealing (Figure S1e–i) for both CID and A-AMI samples. The results confirm that there exists residual  $PbI_2$  in the CID–perovskite film, which was also demonstrated in previous report.<sup>19</sup> It is understandable because the MAI is more difficult to penetrate into the compact  $PbX_2$  film in solid phase. In contrast, the films

prepared by the S-AMI method exhibits pure perovskite phase, intense diffraction peak, larger grains, stronger absorption, and intenser PL intensity, which suggests a complete transformation from wet  $PbX_2$  precursor film to perovskite film with high crystal quality. Prior to coating PCBM, both kinds of perovskite films were annealed at a temperature of  $100 \text{ }^\circ\text{C}$  for varied time for solar cell applications. Notably, the best S-AMI-grown perovskite film was obtained by annealing for  $10 \text{ min}$ , and the annealing optimization procedure will be presented later.

The solar cells were fabricated on FTO glass substrates based on a typical  $p$ – $i$ – $n$  architecture. In this device structure, perovskite layer is sandwiched between PEDOT:PSS hole transport layer and PCBM electron transport layer. Figure 2a shows the devices architecture used in our study. More details about the devices fabrication and perovskite films growth process can be found in the Experimental Section. As a remark, previous reports<sup>27,30</sup> have demonstrated that mixing Cl in the precursor can improve perovskite surface morphology and enhance carrier's diffusion length. The most suitable molar ratio of  $PbI_2:PbCl_2$  in this work has been optimized by incorporating a series of perovskite films grown by CID into solar cells. Obviously, the films surface morphology and devices performance were quite different when different amount of  $PbCl_2$  was introduced (Figures S3 and S4, Tables S1 and S2). These results demonstrate that the devices fabricated from mixed lead halide precursor solution with molar ratios of  $PbI_2:PbCl_2$  at 4:1

and 2:1 showed better performance when the concentration of MAI/IPA solution is fixed at 70 mg/mL, and the best device was obtained using the 4:1 precursor solution of  $\text{PbI}_2\text{:PbCl}_2$ .

Figure 2b shows  $J$ - $V$  curves of devices with active area of  $7.5 \text{ mm}^2$  containing perovskite layers synthesized by S-AMI or CID with different precursor compositions. The main parameters of representative devices are listed in the inset table. Devices fabricated by S-AMI exhibit clearly better performance, especially in terms of short circuit current ( $J_{\text{sc}}$ ) and fill factor (FF). Compared to CID cells,  $J_{\text{sc}}$  increases about  $2.3 \text{ mA/cm}^2$  for the 4:1 group and  $2.1 \text{ mA/cm}^2$  for the 2:1 group. Meanwhile, the FF arises from 73.5% (CID) to 81% (S-AMI) for 4:1 devices and all of devices in the 4:1 S-AMI group. More statistical data in Figure 6 exhibited an impressively high average FF over 80%, and in addition, the highest FF of 82.3% is shown in Figure S5. The typical cross-sectional SEM images of 4:1 S-AMI and 4:1 CID devices are shown in Figure 2c, and cross-sectional SEM images of 2:1 S-AMI and 2:1 CID devices can be seen in Figure S6. Both S-AMI and CID films show similar thickness of around 260 nm, indicating that the S-AMI method has a neglectable impact on the film thickness. The S-AMI film exhibits large grains with size comparable larger than the film thickness, while the perovskite film obtained from CID is composed of many small grains. The charge carriers transport in a single grain without encountering grain boundary leads to lower charge recombination rate and more efficient charge collection for an improved photocurrent and FF,<sup>27</sup> as observed in S-AMI devices.

The  $J$ - $V$  curves of the champion device from 4:1 S-AMI group with forward ( $J_{\text{sc}} \rightarrow V_{\text{oc}}$ ) and reverse ( $V_{\text{oc}} \rightarrow J_{\text{sc}}$ ) scanning are shown in Figure 3a, and the corresponding EQE spectrum can be seen in Figure 3b. No hysteresis is observed with different scanning directions, which has been confirmed in invert structure devices because of the passivation effect from PCBM.<sup>20</sup> This solar cell has a  $J_{\text{sc}}$  of  $22.27 \text{ mA/cm}^2$ , a FF of 79.7%, and an open circuit voltage of 1.02 V and exhibits a high PCE of 18.1% for forward scanning, while the device presents a  $J_{\text{sc}}$  of  $22.18 \text{ mA/cm}^2$ , FF of 81.3%,  $V_{\text{oc}}$  of 1.02 V, and the PCE of 18.3% for reverse scanning. The corresponding EQE value reached 90% at 550 nm and over 80% from 430 to 750 nm. Integrated current density from EQE spectrum is  $21.06 \text{ mA/cm}^2$ , which is very close to the value from the  $J$ - $V$  scanning curves. The  $I$ - $V$  analysis with Shockley equation (Figure S7) indicate that the series resistance of the device is as low as  $0.52 \Omega$ , and the ideal factor is 1.78, which reveals a superb rectification characteristic of the  $p$ - $i$ - $n$  junction.

To gain further insight into the origin of such high device performance, we studied the crystallization process, surface morphology, and photophysics property of both S-AMI and CID films. It should be noted that all of the samples measured were deposited with same parameters as we used for devices fabrication. Figure 4a shows the perovskite film crystallinity changes measured by XRD. The most striking change of these diffraction patterns can be seen as a tendency that the S-AMI-perovskite films get more intense peaks at (110) and (220) plane compared to CID films regardless of the precursor composition of perovskite films. The increased peak intensity reveals that the S-AMI sample possesses increased crystallinity of grains. In addition, other peaks including (200), (211), (202), and (310) almost keep the same for two kinds of films, which confirms that perovskite film deposited by S-AMI has better grain orientation. As shown in Figure 4e, the surface of 4:1 S-AMI-film exhibits a dense and uniform morphology with

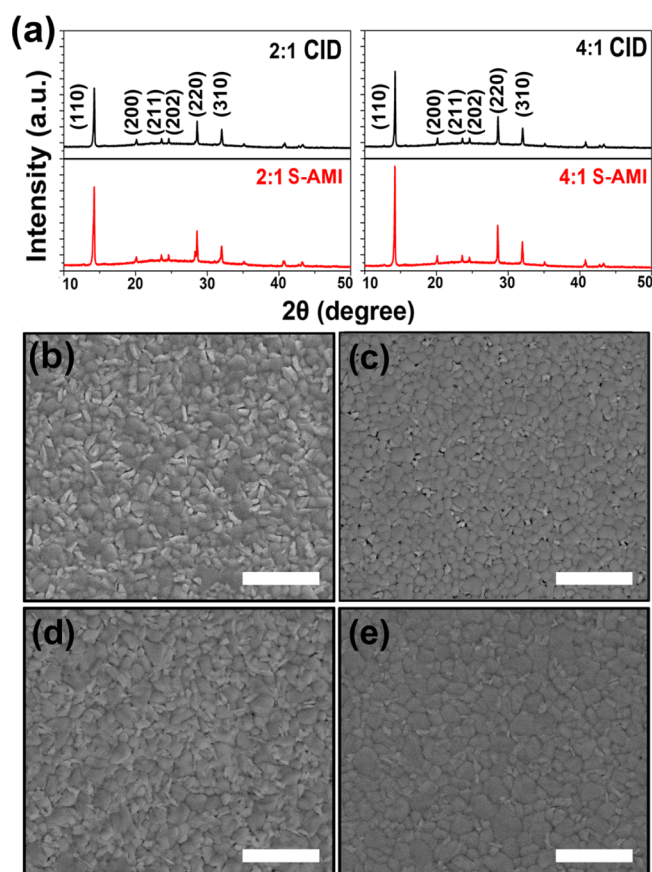


**Figure 4.** (a) XRD patterns of CID-prepared and S-AMI-prepared perovskite films with different composition. (b) SEM image of 2:1 CID, (c) 4:1 CID, (d) 2:1S-AMI, and (e) 4:1 S-AMI. The scale bar is  $2 \mu\text{m}$ .

ordered grains. In contrary, the CID-perovskite film in Figure 4c contains more tiny grains. The same trend can be observed in the 2:1 group film as well (Figure 4b,d). Both XRD and SEM results support that the novel S-AMI deposition method with a DMF wetted  $\text{PbX}_2$  precursor film provides a solvent surrounding to promote the diffusion of precursor ions, which favors MAI molecule to further penetrate into the deeper area of  $\text{PbX}_2$  film. Meanwhile, the rapid assembling of organic and inorganic components in solution provides a direct pathway to form perovskite grains with smaller Gibbs energy, which stimulates grains growth and adjusts the most suitable crystal orientation. In addition, we suggest that benefited from the rapid spreading and penetrating of MAI, perovskite film can grow simultaneously from surface to bottom of the precursor layer, which reduces the surface energy of grains growth and favors crystallites to grow larger, especially along the direction perpendicular to the substrate of device, as shown in Figure 1c. As we all know, grain boundary with disordered structure and defects are detrimental to carrier mobility and inhibits carriers transport and lead free carriers loss through nonradiative recombination. The larger grains with diameter larger than film thickness allow charge carriers to transport across a single crystal without encountering grain boundary in perovskite layer, which decrease the nonradiative recombination rate of photogenerated electrons and holes. This can lead to an improved photocurrent and FF as observed in S-AMI devices (Figure 2a).

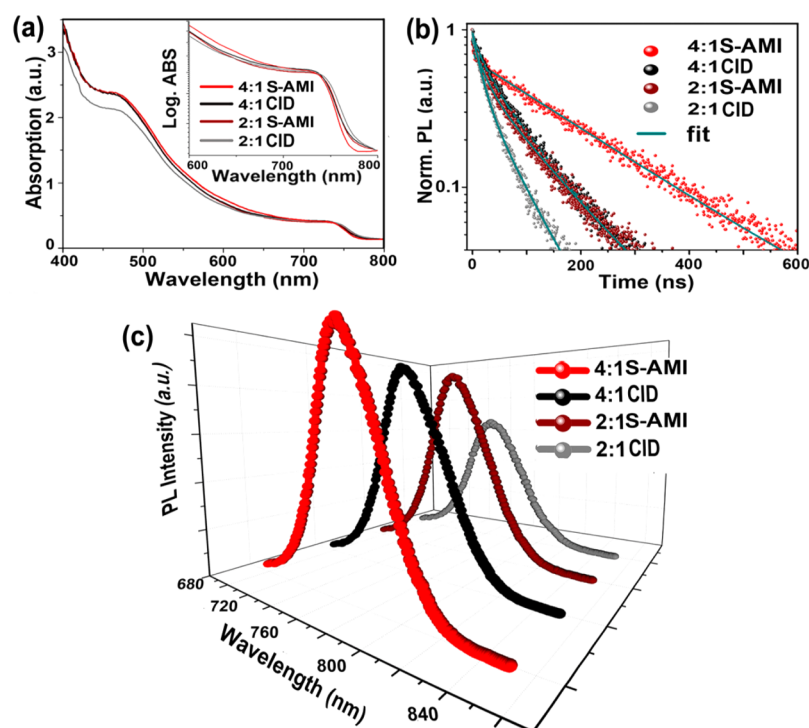


**Figure 5.** (a) UV–vis absorption spectra of different perovskite films synthesized by S-AMI or CID with varied precursor composition; the inset shows the absorption curves with absorption intensity in logarithm scale. (b) Time-resolved photoluminescence spectra of the corresponding perovskite films, where Y-axis symbolizes the normalized PL intensity. A 509.6 nm pulsed diode laser (pulse width: 148.8 ps) with fluence of  $\sim 30$  nJ  $\text{cm}^{-2}$  was used to excite the samples from the glass substrate side. (c) PL spectra of same perovskite films measured for TRPL. All of the S-AMI-prepared samples were subjected to annealing treatment process at 100 °C for 10 min.

The photophysics and electronic property study were conducted to further examine the origin of the efficiency enhancement in the S-AMI devices. Figure 5a displays the absorption of the different perovskite films deposited by S-AMI or CID with varied  $\text{PbX}_2$  composition (4:1 or 2:1). It clearly shows that all samples have similar absorption onset at 770 nm. Compared to CID samples, larger absorption intensity from 450 to 600 nm can be observed for S-AMI films. In addition, the inset spectra in logarithm scale show sharper absorption edges for S-AMI samples. TRPL and steady-state PL were applied to measure the photogenerated charge carriers recombination property. Generally, for a certain perovskite film without quench layer, suppressed nonradiative recombination deriving from less trap states and grain boundary can be determined by longer decay time and larger PL intensity,<sup>30–34</sup> which is preferred for high solar cell device performances. The TRPL spectroscopy was measured using the time-correlated single photon counting (TCSPC) method at a fixed acquisition time, and the perovskite samples were excited from the glass side with a 509.6 nm pulsed diode laser. Figure 5b shows the TRPL spectra of different perovskite layers, and the curves are fitted with the biexponential model<sup>28,34–36</sup>

$$f(t) = \sum a_i e^{-t/\tau_i}, \quad i = 1, 2 \quad (1)$$

where  $a_i$  is a prefactor and  $\tau_i$  is the time constant. The averaged photocarrier recombination lifetime  $\langle \tau \rangle$  is estimated using the  $a_i$  and  $\tau_i$  values from the fitted curves according to eq 2:<sup>28,37</sup>

$$\langle \tau \rangle = \frac{\sum a_i \tau_i^2}{\sum a_i \tau_i}, \quad i = 1, 2 \quad (2)$$

The fitted parameters of TRPL are listed in Table S3 (Supporting Information). The results reveal that the perovskite films deposited by S-AMI present much longer average lifetimes (110 ns for the S-AMI 2:1 device and 212 ns for the S-AMI 4:1 device) than those (61 ns for the CID 2:1 device and 90 ns for the CID 4:1 device) of CID-grown samples. Especially for the 4:1 group films, the CID sample get a lifetime of approximately 90 ns, whereas the lifetime of S-AMI sample increases to  $\sim 212$  ns. Meanwhile, the PL spectra of S-AMI-prepared perovskite films exhibit stronger near-bandgap emission intensity (Figure 5c). Both the TRPL and PL data indicate that the nonradiative recombination is strongly suppressed in the S-AMI films, which mainly benefits from the larger film grains and reduced grain boundary. To further comparing trap density of different perovskite films synthesized by S-AMI and CID, single carrier devices were fabricated with PEDOT:PSS and Au as electrodes, as shown in Figure S8. It has been confirmed that the trap density can be calculated from a marked increase of the current injection at trap-filled limit voltage that is caused by trap filling process with  $V_{\text{TFL}} = en_t L^2 / 2\epsilon\epsilon_0$ .<sup>38</sup> The calculated trap density was  $8.6 \times 10^{15} \text{ cm}^{-3}$  for the S-AMI film and  $1.6 \times 10^{16} \text{ cm}^{-3}$  for the CID film. The results reveal that for the S-AMI film the trap density can be suppressed effectively, which is good for carriers transporting and reduced recombination.

The influences of postannealing on the S-AMI perovskite film quality were also investigated with XRD, SEM, optical absorption, and PL spectrum as shown in Figure S9. We found that the optimized postannealing condition is 100 °C for 10 min, which can remove redundant solvent effectively and is helpful for grains growth. Because of the fast grain formation, the nucleation and growth processes are almost complete when

the S-AMI process is finished. Therefore, longer annealing treatment induces almost no influence on the grains size and crystallinity but leads to perovskite degeneration and generates lots of small  $\text{PbI}_2$  sheets at boundaries, as confirmed in XRD patterns, absorption spectra, and SEM images. The TRPL and steady PL results also indicate that the  $\text{PbI}_2$  produced by overannealing not only increases the recombination of photogenerated carriers but also inhibits charge transport, which seriously affects the film quality of absorption layer and leads to smaller short circuit current density and lower fill factor of the corresponding devices (Figure S10 and Table S4). Moreover, the short annealing time is also an advantage of this novel S-AMI method, which not only significantly simplifies the preparation process but also reduces the energy consuming due to long-term annealing treatment.

Figure 6a–c displays the statistical photovoltaic parameters obtained from more than 30 devices fabricated with same

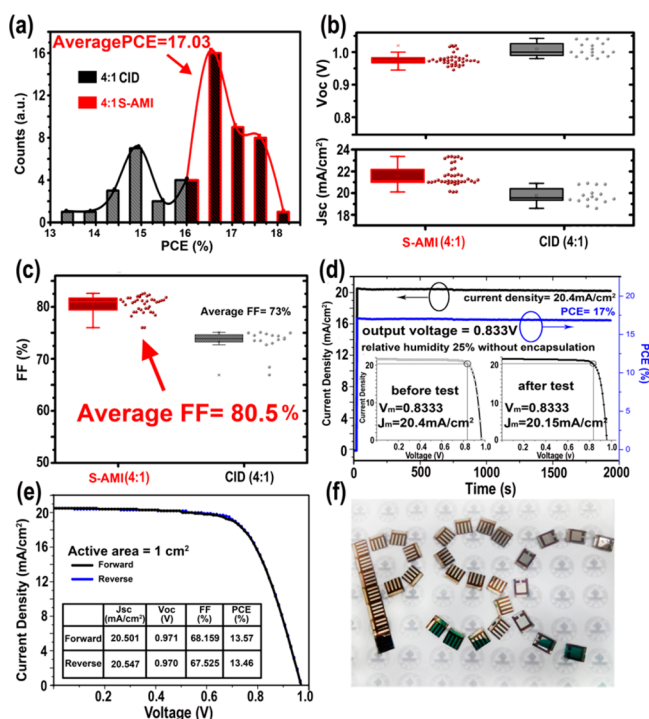


**Figure 6.** (a) Histogram of devices performance obtained from 39 devices. Box plot of the main parameters are displayed in (b)  $J_{sc}$ ,  $V_{oc}$  and (c) FF. (d) Steady-state photocurrent output at the maximum power point (0.833 V). The device  $J$ – $V$  curves before and after output measurements are shown in the inset. (e)  $J$ – $V$  curves of large area (1 cm<sup>2</sup>) device with the best performance; main photovoltaic parameters are listed in the table. All of the  $J$ – $V$  measurements were carried out under ambient atmosphere with relative humidity about 25%. (f) Photographs of real devices (active area 7.5 mm<sup>2</sup> and 1 cm<sup>2</sup>).

precursor (4:1) but different perovskite film deposition method. A clearly enhanced performance is observed for S-AMI devices from Figure 6a, and the average PCE of these devices is about 17%. The PCE enhancement of the S-AMI devices mainly benefits from the enhanced FF from 73% to over 80% (Figure 6c). The statistical histograms of FF,  $J_{sc}$  and  $V_{oc}$  are shown in Figure S11. In order to examine the device stability and output property, we measured the steady-state photocurrent output at the maximum power point (0.833 V) which has been confirmed in the inset of  $J$ – $V$  curve (Figure 6d). The steady-state photocurrent representing the actual

power output of solar cell should be used to accurately characterize the device efficiency; meanwhile, the photo and humidity resistance of the device can be confirmed by a stable photocurrent in a long duration. As shown in Figure 6d, the photocurrent increases to the maximum value in an instant upon illumination with simulated light and the steady-state current fix at 20.4 mA/cm<sup>2</sup> for a long duration over 2000 s. In addition, for the  $J$ – $V$  curves obtained before and after the measurement presented in the inset, there exists almost no change in device performance. It should be noted that the  $I$ – $V$  test was conducted under an ambient atmosphere with relative humidity (RH) about 25%. All devices were measured directly without encapsulation. Then these devices were stored in a drybox (RH about 1%) for long-term stability measurement. The photovoltaic performance evolution of one of our best cells after 49 days is presented in Figure S12 and Table S5. The PCE remains about 77% of its original value, which indicates a commendable long duration stability of the S-AMI-prepared devices.

Finally, we fabricated cells with large active area (1 cm<sup>2</sup>) as an approach to inspect whether this S-AMI method could grow large-size and uniform perovskite film as the cell performance is very sensitive to the active layer. Figure 6e shows the  $J$ – $V$  curve of the best performance cell with quadrate active area of 1 cm<sup>2</sup>. It shows a decent PCE of 13.57% for forward scan and 13.46% for reverse scan. The main photovoltaic parameters are listed in the inset. The PCE statistics of large cells are shown in Table S6. We attribute the decreased FF observed in the large-area cells to the longer carriers across distance among FTO film, which introduces large series resistance. These results give evidence that uniform and large-area perovskite layers with high quality can be grown by S-AMI.

## CONCLUSIONS

We have demonstrated a fast solvent-assisted molecule inserting method based on wet lead halide precursor film without annealing to prepare perovskite film for high performance solar cells. Wet  $\text{PbX}_2$  film with contain amount of DMF provides a direct pathway to form perovskite grains with smaller Gibbs energy, which stimulates grains growth and adjusts the most suitable crystal orientation resulting the perovskite film with dense, large grains and reduced boundaries. Longer carrier lifetime and suppressed trap density of the S-AMI films lead to enhanced devices PCE with high FF over 80%. Meanwhile, these unsealed solar cell devices exhibit good stability in an ambient atmosphere. Moreover, the whole perovskite film fabrication process is shortened within just 10 min. We believe that this novel S-AMI method can be widely employed as a device fabrication platform to explore the photophysics of the new perovskite solar cells.

## ASSOCIATED CONTENT

### Supporting Information

The Supporting Information is available free of charge on the ACS Publications website at DOI: 10.1021/acsami.6b06847.

Pristine perovskite film characterizations including optical images, absorption, PL spectra, XRD and SEM images; precursor composition optimization for perovskite film (SEM and device performance);  $J$ – $V$  curves of the device with the highest fill factor; rectifying analysis with Shockley equation of the champion solar cell device; decay parameters and average lifetime according to a

biexponential fitting model of the PL decay curves obtained for the perovskite films;  $I$ - $V$  curve measured from the PEDOT/perovskite layer/Au sandwich structure; XRD patterns, absorption spectra, PL, TRPL, and devices performance with corresponding EQE spectra of 4:1 S-AMI-prepared perovskite films under different annealing time at 100 °C; statistical histograms of  $J_{sc}$ , FF, and  $V_{oc}$  based on 39 devices (PDF)

## AUTHOR INFORMATION

### Corresponding Author

\*E-mail mse\_caobq@ujn.edu.cn (B.C.).

### Notes

The authors declare no competing financial interest.

## ACKNOWLEDGMENTS

This work is supported by NSFC (51472110) and Shandong Provincial Natural Science Foundation (JQ201214, 2014ZRB01A47). The research project from Ministry of Education, China, is also acknowledged (213021A). B.C. thanks the Taishan Scholar Professorship tenured at University of Jinan.

## REFERENCES

- (1) National Renewable Energy Laboratory (NREL), Best Research-Cell Efficiencies, [http://www.nrel.gov/ncpv/images/efficiency\\_chart.jpg](http://www.nrel.gov/ncpv/images/efficiency_chart.jpg) (accessed: 30th March, 2016).
- (2) Zhou, H.; Chen, Q.; Li, G.; Luo, S.; Song, T.; Duan, H.; Hong, Z.; You, J.; Liu, Y.; Yang, Y. Interface Engineering of Highly Efficient Perovskite Solar Cells. *Science* **2014**, *345*, 542–546.
- (3) Liang, P.; Liao, C.; Chueh, C.; Zuo, F.; Williams, S. T.; Xin, X.; Lin, J.; Jen, A. Additive Enhanced Crystallization of Solution-Processed Perovskite for Highly Efficient Planar-Heterojunction Solar Cells. *Adv. Mater.* **2014**, *26*, 3748–3754.
- (4) Chueh, C.; Liao, C.; Zuo, F.; Williams, S. T.; Liang, P.; Jen, A. The Roles of Alkyl Halide Additives in Enhancing Perovskite Solar Cell Performance. *J. Mater. Chem. A* **2015**, *3*, 9058–9062.
- (5) Li, M.; Liu, L.; Ku, Z.; Liu, T.; Rong, Y.; Xu, M.; Hu, M.; Chen, J.; Yang, Y.; Graetzel, M.; Han, H. A Hole-Conductor-Free, Fully Printable Mesoscopic Perovskite Solar Cell With High Stability. *Science* **2014**, *345*, 295–298.
- (6) Lee, M. M.; Teuscher, J.; Miyasaka, T.; Murakami, T. N.; Snaith, H. J. Efficient Hybrid Solar Cells Based on Meso-Superstructured Organometal Halide Perovskites. *Science* **2012**, *338*, 643–647.
- (7) Chen, Q.; Zhou, H.; Hong, Z.; Luo, S.; Duan, H.; Wang, H.; Liu, Y.; Li, G.; Yang, Y. Planar Heterojunction Perovskite Solar Cells via Vapor-Assisted Solution Process. *J. Am. Chem. Soc.* **2014**, *136*, 622–625.
- (8) Liu, M.; Johnston, B.; Snaith, H. J. Efficient Planar Heterojunction Perovskite Solar Cells by Vapour Deposition. *Nature* **2013**, *501*, 395–398.
- (9) Burschka, J.; Pellet, N.; Moon, S. J.; Humphry-Baker, R.; Gao, P.; Nazeeruddin, M. K.; Graetzel, M. Sequential Deposition as a Route to High-Performance Perovskite-Sensitized Solar Cells. *Nature* **2013**, *499*, 316–319.
- (10) Jeng, J. Y.; Chiang, Y.; Lee, M. H.; Peng, S.; Guo, T.; Chen, P.; Wen, T.  $\text{CH}_3\text{NH}_3\text{PbI}_3$  Perovskite/Fullerene Planar-Heterojunction Hybrid Solar Cells. *Adv. Mater.* **2013**, *25*, 3727–3732.
- (11) Luo, P.; Liu, Z.; Xia, W.; Yuan, C.; Cheng, J.; Lu, Y. Uniform, Stable, and Efficient Planar-Heterojunction Perovskite Solar Cells by Facile Low-Pressure Chemical Vapor Deposition under Fully Open-Air Conditions. *ACS Appl. Mater. Interfaces* **2015**, *7*, 2708–2714.
- (12) Eperon, G. E.; Burlakov, V. M.; Docampo, P.; Goriely, A.; Snaith, H. J. Morphological Control for High Performance, Solution-Processed Planar Heterojunction Perovskite Solar Cells. *Adv. Funct. Mater.* **2014**, *24*, 151–157.
- (13) Longo, G.; Escrig, L.; Gil, Degen, M. J.; Sessolo, M.; Bolink, H. J. Perovskite Solar Cells Prepared by Flash Evaporation. *Chem. Commun.* **2015**, *51*, 7376–7378.
- (14) Shi, J.; Luo, Y.; Wei, H.; Luo, J.; Dong, J.; Lv, S.; Xiao, J.; Xu, Y.; Zhu, L.; Xu, X.; Wu, H.; Li, D.; Meng, Q. Modified Two-Step Deposition Method for High-Efficiency  $\text{TiO}_2/\text{CH}_3\text{NH}_3\text{PbI}_3$  Heterojunction Solar Cells. *ACS Appl. Mater. Interfaces* **2014**, *6*, 9711–9718.
- (15) Xiao, M.; Huang, F.; Huang, W.; Yasmina, D.; Zhu, Y.; Etheridge, J.; Weale, A. G.; Bach, U.; Cheng, Y.; Spiccia, L. A Fast Deposition-Crystallization Procedure for Highly Efficient Lead Iodide Perovskite Thin-Film Solar Cells. *Angew. Chem.* **2014**, *126*, 10056–10061.
- (16) Pang, S.; Zhou, Y.; Wang, Z.; Yang, M.; Amanda, R. K.; Zhou, Z.; Zhu, K.; Padture, Nitin, P.; Cui, G. Transformative Evolution of Organolead Triiodide Perovskite. Thin Films from Strong Room-Temperature Solid-Gas Interaction between  $\text{HPbI}_3$ - $\text{CH}_3\text{NH}_2$  Precursor Pair. *J. Am. Chem. Soc.* **2016**, *138*, 750–753.
- (17) Ahn, N.; Son, D. Y.; Jang, I. H.; Kang, S.; Choi, M.; Park, N. G. Highly Reproducible Perovskite Solar Cells with Average Efficiency of 18.3% and Best Efficiency of 19.7% Fabricated via Lewis Base Adduct of Lead (II) Iodide. *J. Am. Chem. Soc.* **2015**, *137*, 8696–8699.
- (18) Jeon, N. J.; Noh, J. H.; Kim, Y. C.; Yang, W. S.; Ryu, S. C.; Seok, S. Solvent Engineering for High-Performance Inorganic–Organic Hybrid Perovskite Solar Cells. *Nat. Mater.* **2014**, *13*, 897–903.
- (19) Xiao, Z.; Bi, C.; Shao, Y.; Dong, Q.; Wang, Q.; Yuan, Y.; Wang, C.; Gao, Y.; Huang, J. Efficient High Yield Perovskite Photovoltaic Devices Grown by Interdiffusion of Solution-Processed Precursor Stacking Layers. *Energy Environ. Sci.* **2014**, *7*, 2619–2623.
- (20) Bi, C.; Yuan, Y.; Fang, Y.; Huang, J. Low-Temperature Fabrication of Efficient Wide-Bandgap Organolead Trihalide Perovskite Solar Cells. *Adv. Energy. Mater.* **2015**, *5*, 1401616.
- (21) You, J.; Meng, L.; Song, T.; Guo, T.; Yang, Y.; Chang, W.; Hong, Z.; Chen, H.; Zhou, H.; Chen, Q.; Liu, Y.; De Marco, N.; Yang, Y. Improved Air Stability of Perovskite Solar Cells via Solution-Processed Metal Oxide Transport Layers. *Nat. Nanotechnol.* **2015**, *11*, 75–81.
- (22) Xiao, Z.; Yuan, Y.; Wang, Q.; Shao, Y.; Bai, Y.; Deng, Y.; Dong, Q.; Hu, M.; Bi, C.; Huang, J. Thin-Film Semiconductor Perspective of Organometal Trihalide Perovskite Materials For High-Efficiency Solar Cells. *Mater. Sci. Eng., R* **2016**, *101*, 1–38.
- (23) Wu, C.; Chiang, C.; Tseng, Z.; Hagfeldt, A.; Gratzel, M. High Efficiency Stable Inverted Perovskite Solar Cells Without Current Hysteresis. *Energy Environ. Sci.* **2015**, *8*, 2725–2733.
- (24) Chiang, C.; Wu, C. Bulk Heterojunction Perovskite-PCBM Solar Cells with High Fill Factor. *Nat. Photonics* **2016**, *10*, 196–200.
- (25) Li, W.; Fan, J.; Li, J.; Mai, Y.; Wang, L. Controllable Grain Morphology of Perovskite Absorber Film by Molecular Self-Assembly toward Efficient Solar Cell Exceeding 17%. *J. Am. Chem. Soc.* **2015**, *137*, 10399–10405.
- (26) Xiao, Z.; Wang, D.; Dong, Q.; Wang, Q.; Wei, W.; Dai, J.; Zeng, X.; Huang, J. Unraveling the Hidden Function of a Stabilizer in a Precursor in Improving Hybrid Perovskite Thin Morphology for High Efficiency Solar Cell. *Energy Environ. Sci.* **2016**, *9*, 867–872.
- (27) Dong, Q.; Yuan, Y.; Shao, Y.; Fang, Y.; Wang, Q.; Huang, J. Abnormal Crystal Growth in  $\text{CH}_3\text{NH}_3\text{PbI}_{3-x}\text{Cl}_x$  using a Multi-Cycle Solution Coating Process. *Energy Environ. Sci.* **2015**, *8*, 2464–2470.
- (28) Yuan, S.; Qiu, Z.; Zhang, H.; Gong, H.; Hao, Y.; Cao, B. Oxygen Influencing The Photocarriers Lifetime of  $\text{CH}_3\text{NH}_3\text{PbI}_{3-x}\text{Cl}_x$  Film Grown by Two-Step Interdiffusion Method and Its Photovoltaic Performance. *Appl. Phys. Lett.* **2016**, *108*, 033904.
- (29) Xiao, Z.; Dong, Q.; Bi, C.; Shao, Y.; Yuan, Y.; Huang, J. Solvent Annealing of Perovskite-Induced Crystal Growth for Photovoltaic-Device Efficiency Enhancement. *Adv. Mater.* **2014**, *26*, 6503–6509.
- (30) Stranks, S. D.; Eperon, G. E.; Grancini, G.; Menelaou, C.; Alcocer, M.; Leijtens, T.; Herz, L. M.; Petrozza, A.; Snaith, H. J. Electron-Hole Diffusion Lengths Exceeding 1 Micrometer in an Organometal Trihalide Perovskite Absorber. *Science* **2013**, *342*, 341–343.

(31) You, J.; Yang, Y.; Hong, Z.; Song, T.; Meng, L.; Liu, Y.; Jiang, C.; Zhou, H.; Chang, W.; Li, G.; Yang, Y. Moisture Assisted Perovskite Film Growth for High Performance Solar Cells. *Appl. Phys. Lett.* **2014**, *105*, 183902.

(32) DeQuilettes, D. W.; Vorpahl, S. M.; Stranks, S. D.; Nagaoka, H.; Eperon, G. E.; Ziffer, M. E.; Snaith, H. J.; Ginger, D. S. Impact of Microstructure on Local Carrier Lifetime in Perovskite Solar Cells. *Science* **2015**, *348*, 683–686.

(33) Stranks, S. D.; Burlakov, V. M.; Ball, J. M.; Goriely, A.; Snaith, H. J. Recombination Kinetics in Organic-Inorganic Perovskites: Excitons, Free Charge, and Subgap States. *Phys. Rev. Appl.* **2014**, *2*, 034007.

(34) Yang, D.; Yang, R.; Zhang, J.; Yang, Z.; Liu, S.; Li, C. High Efficiency Flexible Perovskite Solar Cells using Superior Low Temperature TiO<sub>2</sub>. *Energy Environ. Sci.* **2015**, *8*, 3208–3214.

(35) James, D. R.; Liu, Y.; De Mayo, P.; Ware, W. R. Distributions of Fluorescence Lifetimes: Consequences for the Photophysics of Molecules Adsorbed on Surfaces. *Chem. Phys. Lett.* **1985**, *120*, 460–465.

(36) Carrero, S. G.; Galian, R. E.; Prieto, J. P. Maximizing the Emissive Properties of CH<sub>3</sub>NH<sub>3</sub>PbBr<sub>3</sub> Perovskite Nanoparticles. *J. Mater. Chem. A* **2015**, *3*, 9187–9193.

(37) Bube, R. H. Trap Density Determination by Space-Charge-Limited Currents. *J. Appl. Phys.* **1962**, *33*, 1733–1737.

(38) Dong, Q.; Fang, Y.; Shao, Y.; Mulligan, P.; Qiu, J.; Cao, L.; Huang, J. Electron-Hole Diffusion Lengths > 175 μm in Solution-Grown CH<sub>3</sub>NH<sub>3</sub>PbI<sub>3</sub> Single Crystals. *Science* **2015**, *347*, 967–970.